



# Failure mode of the hazardous Diaozui rock mass of the Qutang Gorge in the Three Gorges Reservoir area based on a three-dimensional numerical analysis

Haiyou Peng<sup>1,2,3</sup> · Qiang Xie<sup>1</sup> · Bolin Chen<sup>1,2,3</sup> · Kang Tan<sup>2,3</sup> · Zhilin Cao<sup>1</sup> · Bin Wu<sup>2,3,4</sup>

Received: 5 July 2023 / Accepted: 25 February 2024  
© The Author(s) 2024

## Abstract

The occurrence of rockfalls is a prevalent geological hazard, especially in the Three Gorges Reservoir area of the Yangtze River. Analyzing the pre-rockfall evolution process of hazardous rock mass is crucial for stability assessment, risk monitoring, and evaluation. Generally, numerical analysis is conducted to study the rock stability and failure; however, it is primarily based on the two-dimensional calculation of typical cross-sections without considering the shape of the three-dimensional space of the hazardous rock mass, thus leading to distorted results. To address this issue, this paper proposes a methodological approach for the analysis of the stability conditions of a hazardous rock mass. The approach starts with field investigations and an Unmanned aerial vehicle (UAV) photogrammetric survey to gather data. These data are then used to construct a three-dimensional (3D) geological model of rock mass. Finally, a 3D numerical simulation is performed to analyse the potential failure processes of hazardous rock mass. In this study, we focused on the hazardous Diaozui rock mass of the Qutang Gorge in the Three Gorges Reservoir area (China). We constructed a 3D geological model of the rock mass based on the data from the field survey and UAV photogrammetric survey. Using this 3D geological model, we established a 3D numerical analysis model to assess the rockfall hazard. By utilizing the Strength reduction method (SRM) and simulating the collapse process of the hazardous rock mass, we analyzed the instability mechanism and failure evolution process of the Hazardous Diaozui rock mass. The results illustrated the potential failure mode, the key-oriented wedges of the rock mass, and the potential critical failure point for the hazardous rock mass. These findings provide valuable insights for stability assessment, risk monitoring, and evaluation of the hazardous rock mass in the Three Gorges Reservoir area.

**Keywords** Hazardous rock mass · Rockfall · Three Gorges Reservoir area · Numerical analysis · Failure mode

## Introduction

Hazardous rock mass exists on an overhanging slope or a steep cliff. Rockfall, characterized by its complex causes and low predictability, is a global geological disaster and has caused mass casualties and huge economic losses worldwide, including in Hokkaido Island in Japan, the Swiss Alps, Brazil, India, Italy, and China (Azzoni and de Freitas 1995; Antoniou and Lekkas 2010; Abu Seif and Bahabri 2019; Verma et al. 2019; Pignalosa et al. 2022). There are large quantities of high and steep rock mass in the Three Gorges Reservoir area of China (Bolin et al. 2010). If a rock mass collapses and falls into the river, the rockfall-generated impulse waves cause massive damage and even overturn the vessels (Huang et al. 2012, 2019; Wang et al. 2017; Zhang et al. 2020). On November 23, 2008, a rockfall occurred in Gongjiafang, Wushan County in the Three Gorges Reservoir

✉ Qiang Xie  
xieqiang2000@cqu.edu.cn

<sup>1</sup> School of Civil Engineering, Chongqing University, Chongqing 400045, People's Republic of China

<sup>2</sup> Technology Innovation Center of Geohazards Automatic Monitoring, Ministry of Natural Resources (Chongqing Institute of Geology and Mineral Resources), Chongqing 401120, People's Republic of China

<sup>3</sup> Chongqing Engineering Research Center of Automatic Monitoring for Geological Hazards (Chongqing Institute of Geology and Mineral Resources), Chongqing 401120, People's Republic of China

<sup>4</sup> Chongqing Industry Polytechnic College, Chongqing 401120, People's Republic of China

area of Chongqing and approximately 380,000 m<sup>3</sup> of rocks sliding into the river generated a surge height of 13 m (Huang et al. 2012). On October 20, 2011, Wangxia rock mass with a volume of more than 50,000 m<sup>3</sup> collapsed in the Wushan County in the Three Gorges Reservoir area of Chongqing, seriously threatening the navigation safety in the Yangtze River waterways (Feng et al. 2014). On October 8, 2017, a rock mass of approximately 7000 m<sup>3</sup> from the Fenghuang Mountain collapsed, with half of them entering the Daning River and causing a surge height of 2.0 m. There is a high risk of rockfall in the Three Gorges Reservoir area (Yin et al. 2016). To minimize this risk, the study of the failure evolution of hazardous rock mass is highly essential to analyse the rock stability as well as the evaluation and monitoring of a rockfall.

Scholars have conducted numerous studies on rockfall, primarily focusing on the mechanism of formation of hazardous rock mass (Zheng et al. 2015; Mavrouli and Corominas 2017; Wang et al. 2020b); the calculation and evaluation of rock stability, rockfall trajectory and range of damage (Pignalosa et al. 2022; Yan et al. 2023), and the risk of rockfall (Abu Seif and Bahabri 2019; Menk et al. 2023); and rockfall monitoring and prevention (Lambert and Bourrier 2013; Perera and Lam 2023). Numerical analysis is an effective research approach, generally applied to study the stability and failure mode of hazardous rock mass (Feng et al. 2014; Verma et al. 2019). However, this analysis mainly focuses on the two-dimensional calculation of a model based on the typical cross-sections of hazardous rock mass owing to the difficulty in obtaining data on the spatial shape and fissure surface of the rock mass as well as the currently available immature three-dimensional modeling technology for developing a model of rock mass (Singh et al. 2013; Wang et al. 2020a, b). Hence, the analysis results tend to be distorted to a certain extent. In recent years, Unmanned aerial vehicle (UAV) photography, airborne remote sensing, and aircraft radar have been applied to the survey of hazardous rock mass, including fissure identification and feature analysis (Congress and Puppala 2021; Farmakis et al. 2022; Schilirò et al. 2022; Wang et al. 2022; Zhang et al. 2022). The use of technologies, such as three-dimensional tilt photography, makes it easier to obtain three-dimensional images of the rock mass and their surface point cloud data. Hence, establishing a realistic three-dimensional model of hazardous rock mass becomes feasible (Daghigh et al. 2022). Usually, a method for identifying discontinuity rock mass surface based on point cloud data is used to construct a rock mass 3D surface model (Umili et al. 2013; Li et al. 2016), alternatively, the method of identifying discontinuity rock mass surface and analyzing geometric features using UAV (Menegoni et al. 2019; Zhang et al. 2022).

In this study, we obtained the three-dimensional spatial data of hazardous rock mass in the Diaozui rockfall-prone

mass of the Qutang Gorge in the Three Gorges Reservoir area through site survey and tilt photography. Using the data obtained, we constructed a three-dimensional geological model of the hazardous rock mass, based on which a three-dimensional numerical analysis model was established. Numerical analysis of the failure evolution process of hazardous rock mass was conducted using the SRM and simulating the collapse process of hazardous rock mass. The instability mechanism of hazardous rock mass was analyzed to illustrate their potential failure mode.

## Background of the study area

### Characteristics of the Diaozui rock-prone mass

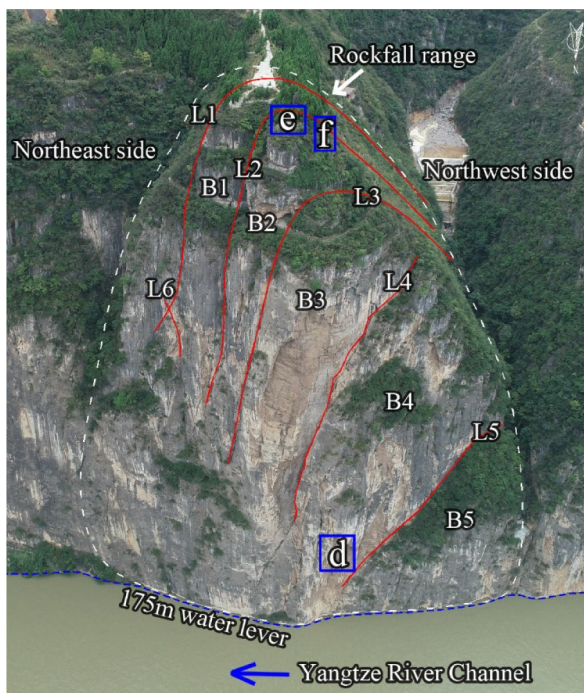
The hazardous Diaozui rock mass is located in the Three Gorges Reservoir area of the Yangtze River approximately 1 km away from the upstream entrance of the right bank of the Qutang Gorge of the Yangtze River (Fig. 1a). They primarily consist of nearly vertical cliffs and some inverted cliffs, with gullies along their left and right sides. Their free-face slopes face the Yangzi River with penetrating fissures. The elevation of the hazardous rock mass ranges from 143 to 401 m, with a relative elevation difference of 258 m, higher in the south and lower in the north. The left side inclines to the northwest side by approximately 320°, with a width of about 120 m. The right side inclines to the northeast side by about 40°, with a width of approximately 110 m. The river is about 380 m wide (Fig. 1b).

The hazardous Diaozui rock mass is situated on the northern flank of the Qiyao Mountain Anticline. It is devoid of any nearby faults. The bedrock consists of gray to gray-white limestone and dolomitic limestone belonging to the Triassic system's Jialingjiang formation (T<sub>1j2</sub>), and the thickness of these layers ranges from 5 to 46 cm, with horizontal bedding and a rock layer attitude of 350°~1°<9°~12°. Two sets of fractures, namely LX1 and LX2, are present within the rock mass. The LX1 fractures have a dip direction ranging between 158 and 170°, with a dip angle between 65 and 85°. They extend approximately 68 to 130 m in length, with a spacing of 0.5 to 6 m. These fractures are relatively straight and possess an opening width of 0.5 to 2.5 m. LX1 can be characterized as a hard structural plane, partially filled with rock debris and blocks, exhibiting a poor bonding degree. LX2 fractures have a dip direction ranging between 70 and 97°, with a dip angle between 76 and 86°. They extend approximately 15 to 70 m in length, with a spacing of 0.2 to 3 m. LX2 is a hard structural plane that is relatively rough, slightly open, and lacks filling material, exhibiting a poor bonding degree.

Through the field survey and UAV tilt photography, we found five long, wide, and penetrating fissures on the northeast side of



(a) Location of hazardous Diaozi rockfall mass



(b) North side of Diaozi rock mass



(c) Northeast side of Diaozi rock mass



(d) Falling of rock mass under pressure



(e) Ground fissure (DL NO.1)



(f) Ground fissure (DL NO.2)

Fig. 1 Location and characteristics of the hazardous Diaozi rock mass

the cliff and gullies on the southwest side. They are denoted as L1–L5, with a maximum extension length of 167 m, an opening width of 0.5–2.5 m, and a fissure spacing of 15–26 m (Fig. 1b and c). All the hazardous Diaozui rock mass was divided into five plate-like parts by the five penetrating fissures, which are denoted as B1, B2, B3, B4, and B5 from the inner part to the outer part of the rock mass, respectively (Fig. 1b and c). Each rock plate is 11.8–25.0 m thick, 71.6–120.0 m wide, and 84–167.0 m high, with a volume of  $17.36 \times 10^4$ – $33.46 \times 10^4$  m<sup>3</sup>. The total volume of the hazardous Diaozui rock mass is  $127.41 \times 10^4$  m<sup>3</sup>, being one of the largest hazardous rock masses. The rock mass is inclined to collapse along their inverted slopes at about 320° to the northwest. There is a short fracture, denoted as L6, at the bottom of B1.

### Recent deformation

On July 27, 2022, the surface of the hazardous Diaozui rock mass partially collapsed. Rocks fell into the Yangtze River waterway, attracting people's attention to its potential hazard. Recently, several collapses of different scales (ranging from 1 to 3600 m<sup>3</sup>) have also occurred on the cliff surface (Fig. 1d). A cliff-top viewing platform was built in 2018, and a ground fissure occurred on this platform. This fissure, denoted as DL1, extends at 55° and runs through the entire viewing platform, with an extended length of 12 m and an opening width of 0–3 cm (Fig. 1e). The railings on the west side of the viewing platform and the pavement of the footpath are also deformed due to the fissures (Fig. 1f). The potential risk of rockfall in this area directly threatens the navigation safety of the Yangtze River owing to the great volume of rock mass. Furthermore, follow-up disasters, including swells, can cause severe damage to towns, docks, and ships in Fengjie.

## Research approaches

### Methods and procedure

We studied the failure evolution process of Diaozui rock mass using a three-dimensional numerical analysis. Since the introduction of the SRM in 1975 by Zienkiewicz et al. (1975), it has been increasingly applied for analyzing the stability of the rock mass and rock slopes (Sun et al. 2016; Yang et al. 2021a, b; Zheng et al. 2009). We applied the SRM to calculate the displacement and distribution of the plastic zone of Diaozui rock mass when the strength reduction reached the limit state for analyzing the failure mode. The workflow of the hazardous rock mass three-dimensional numerical analysis has been shown in Fig. 2. The methods and procedure are performed as follows:

(1) Investigation and surveying: Obtain information on fractures of Diaozui rock mass through investigation

and mapping, including fracture's attitude, location, and length. Obtaining images and spatial coordinates of Diaozui rock mass surfaces through UAV tilt photography.

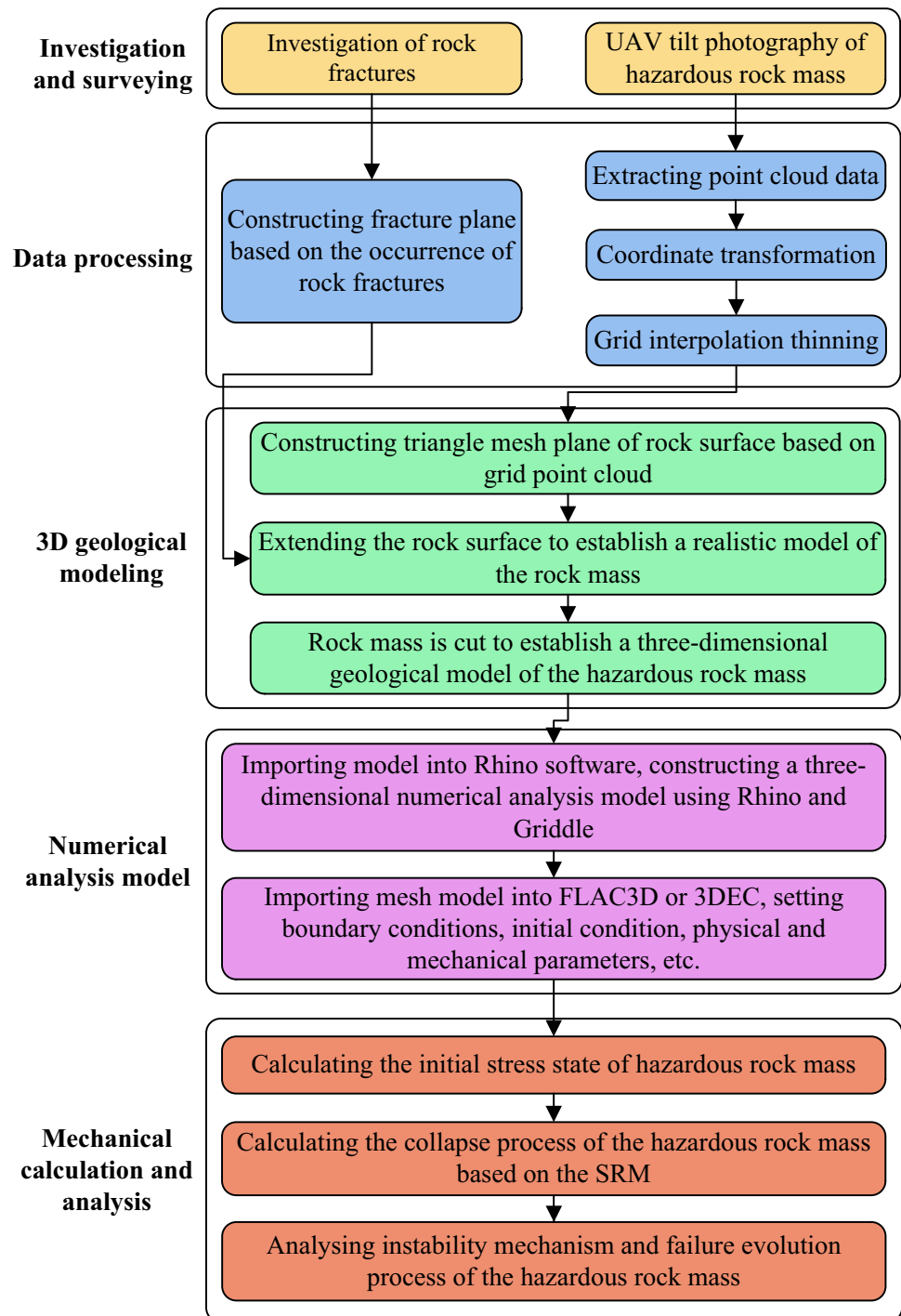
- (2) Data processing: This step aims to process survey and UAV tilt photography data to facilitate the construction of a three-dimensional geological model. Specifically, point cloud data capturing the characteristics of the rock surface were acquired through UAV tilt photography. Subsequently, the spatial coordinates of these points were transformed, and grid interpolation thinning was conducted to reduce the density of the point cloud data. Additionally, it is essential to establish a plane equation for the fissure plane of the Diaozui rock mass, taking into consideration the orientation and spatial relationship of the rock fractures.
- (3) 3D geological modeling: The processed grid point cloud data was utilized to create a triangle mesh representation of the rock surface. This triangle mesh was then expanded to generate a realistic model of the entire rock mass. Furthermore, the rock mass was dissected by the fissure plane to establish a comprehensive three-dimensional geological model of the hazardous rock mass.
- (4) Numerical analysis modeling: A three-dimensional numerical analysis model of the hazardous rock mass is developed using the geological model as a basis. The geological model is imported into Rhino software and subsequently meshed using Rhino and Griddle. Finally, the meshed model is imported into FLAC3D or 3DEC for the finalization of model configurations.
- (5) Mechanical calculation and analysis: Firstly, the initial stress field of the model should be calculated. Then, it is necessary to compare and analyse the calculation results with the deformation characteristics of Diaozui rock mass to verify the correctness of the numerical analysis model. Finally, the SRM and the collapse process simulation of the rock mass were applied to analyse their instability mechanism and failure evolution process.

### Investigation and surveying

We constructed the three-dimensional shape of the rock mass surface (riverside face). Specifically, DJI Jingwei 300RTK with the Zenmuse P1 camera was used for close-range photogrammetry of the survey area, with a distance shorter than 8 m. After collecting the photograph, we established a realistic three-dimensional model by cluster computing, based on which discrete point cloud data of the rock surface was extracted.

There are five main vertical fractures on the Diaozui rock mass, namely L1, L2, L3, L4, and L5, which were respectively generalized into a plane. They cut the

**Fig. 2** The workflow of the hazardous rock mass three-dimensional numerical analysis



Diaozui rock mass into five rock blocks. From the three-dimensional data obtained through tilt photography, we obtained a point  $(x_0, y_0, \text{ and } z_0)$  in the three-dimensional space. Combined with the rock structural attitude obtained from the field survey, we obtained the parameters of the fracture surface. The spatial information of the fractures L1, L2, L3, L4, and L5 in an independent coordinate system is shown in Table 1.

**Data processing**

**UAV tilt photography point cloud processing**

Because we could not directly apply the data for geological modeling and numerical calculation owing to its great amount and uneven distribution, and thus, the point cloud data required processing.

**Table 1** The spatial information of the fractures

Fracture no.	Coordinate of a point on the fracture plane			Dip direction	Dip angle
	x (m)	y (m)	z (m)		
L1	172.90	203.48	306.00	154.00	88.00
L2	156.01	216.22	332.00	154.00	86.00
L3	149.34	226.66	296.00	154.00	85.00
L4	128.19	238.02	253.00	154.00	84.00
L5	79.13	245.06	218.00	154.00	82.00

We applied Kriging interpolation to process the point cloud data. As the three-dimensional surface of the rock is concave–convex, the three-dimensional point cloud data may have multiple corresponding  $z$  values in the plane  $x$  and  $y$  coordinates; therefore, errors can occur when using Kriging interpolation directly. To solve this problem, we adopted a coordinate transformation approach, making each pair of  $x$  and  $y$  in the transformed three-dimensional point cloud of the rock surface correspond only to the unique  $z$  coordinate. As shown in Fig. 3, under the original coordinate system ( $x$ ,  $y$ , and  $z$ ), the included angle between the primary rock collapse direction (representing the protruding direction of the rock mass) and the  $y$ -axis is  $\alpha$ . We followed Formula (1) to transform the three-dimensional point cloud number of the rock surface. After the transformation, the primary collapse direction of the rock surface was transformed into the  $z$ -axis, and point cloud coordinates of the rock mass surface under the new coordinate system ( $x'$ ,  $y'$ , and  $z'$ ) were obtained. Under the new coordinate system, each pair of  $x$  and  $y$  corresponded to only one  $z$  value. Thus, the Kriging interpolation approach was applicable.

$$\begin{cases} x' = z \\ y' = (x + \Delta x)\cos\alpha + (y + \Delta y)\sin\alpha \\ z' = -(x + \Delta x)\sin\alpha + (y + \Delta y)\cos\alpha \end{cases} \quad (1)$$

where  $\Delta x$  and  $\Delta y$  are coordinate transformation values.

A grid point cloud with a spacing of 1 m was thinned out during Kriging interpolation, based on which a Delaunay model of the rock-free face was established, as shown in Fig. 4. The model clarified the shape of the three-dimensional space of the rock surface, especially the rock cavities (marked in red boxes in Fig. 4d). These cavities play a cortical role in the local stress variation of the rock mass, which further influences the overall stability of the rock mass.

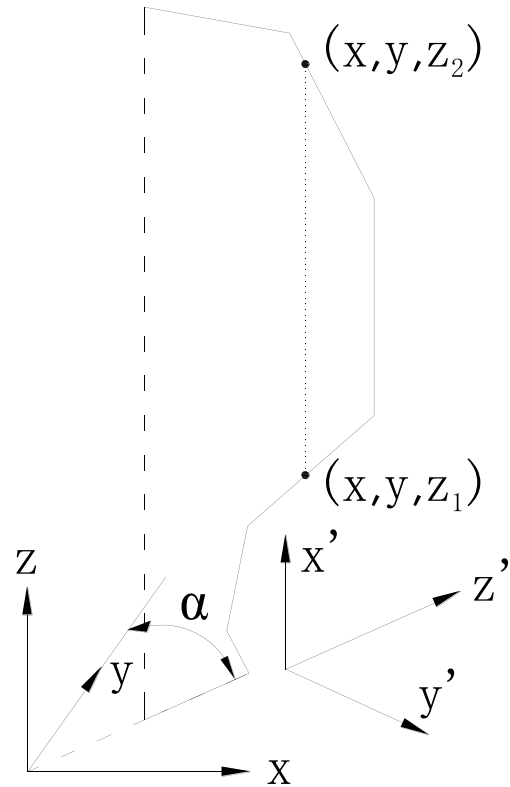


**Fig. 3** Scheme of coordinate system transformation of the rock-surface point cloud data

**Fissures equation**

According to the point ( $x_0$ ,  $y_0$ , and  $z_0$ ) in the three-dimensional space of the structural plane, the plane dip direction  $\theta$ , and the dip angle  $\varphi$ , the structural plane equation can be formulated; the unit normal vector of the structural plane is given as  $(\cos\theta, \sin\theta, \text{and } 1/\tan\varphi)$ . The plane equation of rock fractures can be expressed as follows:

$$\cos\theta(x - x_0) + \sin\theta(y - y_0) + \frac{1}{\tan\varphi}(z - z_0) = 0 \quad (2)$$

Therefore, we established plane equations of the main fissures L1, L2, L3, L4, and L5. As shown in Eqs. (3), (4), (5), (6), and (7) respectively.

$$-0.9(x - 172.90) - 0.44(y - 203.48) + 0.035(z - 306.0) = 0 \quad (3)$$

$$-0.9(x - 156.01) - 0.44(y - 216.22) + 0.070(z - 332.0) = 0 \quad (4)$$

$$-0.9(x - 149.34) - 0.44(y - 226.66) + 0.087(z - 296.0) = 0 \quad (5)$$

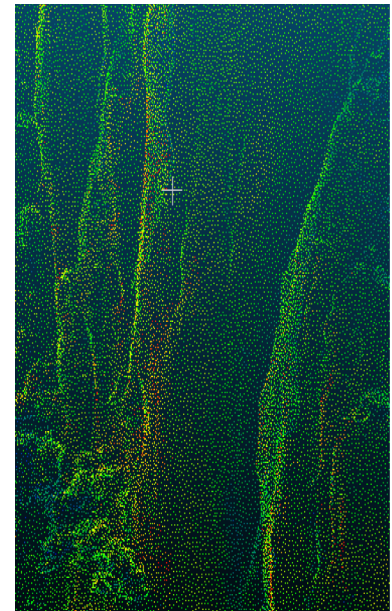
$$-0.9(x - 128.19) - 0.44(y - 238.02) + 0.105(z - 253.0) = 0 \quad (6)$$

$$-0.9(x - 79.13) - 0.44(y - 245.06) + 0.141(z - 218.0) = 0 \quad (7)$$

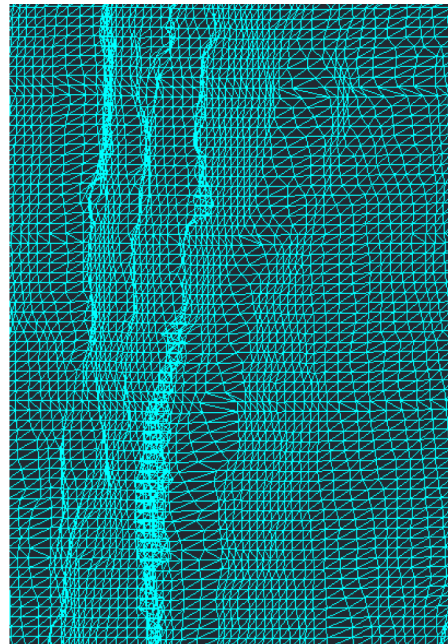
**Fig. 4** Modeling of the rock surface based on UAV tilt photography



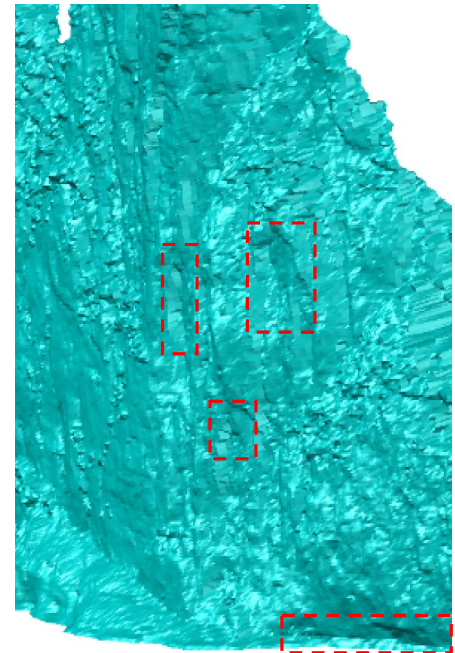
(a) UAV tilt photography of the rock mass surface.



(b) Point cloud data of the rock mass surface.



(c) Triangle mesh surface of the rock mass surface.



(d) The rock mass surface model.

### Three-dimensional geological modeling

A geological model of the Diaozui rock mass was developed by integrating the Delaunay model of the rock surface and the gully planes on the west and east sides, as shown in Fig. 5a. The structural planes of the main fissures L1, L2, L3, L4, and L5 were generalized into a plane. Furthermore, we developed a single model for B1, B2, B3, B4, and B5 by dividing the realistic three-dimensional geological model of Diaozui rock mass according

to the main fissure plane. Therefore, the volume and weight of the five rock blocks are obtained, as shown in Table 2. Finally, the three-dimensional geological model of the Diaozui rock mass was established, as shown in Fig. 5b.

### Numerical analysis model

We are mainly concerned about the stress-strain process before the failure of the Diaozui rock mass. In terms of rock

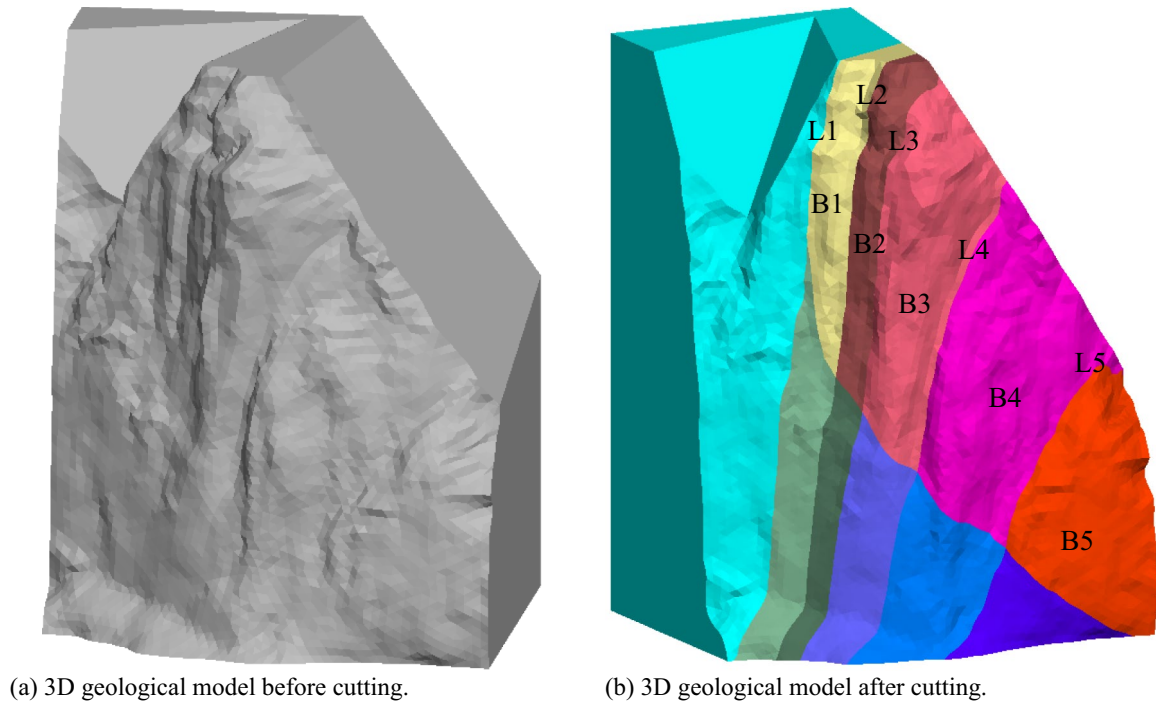


Fig. 5 3D geological model of the Diaozui rock mass

Table 2 Information of the rock blocks

Rock blocks NO.	B1	B2	B3	B4	B5
Volume (10 <sup>4</sup> m <sup>3</sup> )	23.71	21.59	33.46	31.29	17.36
Rock block weight (10 <sup>4</sup> kN)	616.52	561.40	870.20	813.70	451.48
Rock block morphology					

mass structural planes, only the five major controlling fractures of the Diaozui rock mass are considered. The detachment of the five rock blocks is not taken into consideration. Therefore, for this study, the continuum mechanics analysis software FLAC3D was chosen as the simulation software.

To construct a numerical analysis grid model, the data of the 3D geological model of the Diaozui rock mass is imported into Rhino software. The model is then meshed using Rhino and Griddle software to meet the simulation requirements. With a focus on achieving both computational accuracy and speed, we have set the mesh grid size to 4 m. The resulting model consists of 1,696,485 zones and 291,337 grid points.

We developed a realistic numerical analysis model by importing the three-dimensional geological model of the Diaozui rock mass into the numerical analysis software FLAC<sup>3D</sup>. We performed mesh division on the analysis model to develop the finite-difference mesh calculation model, which was optimized by setting the boundary conditions, initial conditions, geotechnical mechanical parameters, and constitutive model, as shown in Fig. 6. The elevation of the model's bottom was 146.5 m and the elevation of the model's top, that is, the Diaozui viewing platform, was 249.2 m, with an elevation of about 395.7 m. The model was 249.2 m high, 200.0 m wide, and 150.0 m deep. The realistic unit

model was used for simulating the main body of the rock mass, whereas the interface unit was applied for simulating the fissure surfaces on the rock mass.

The Mohr–Coulomb model is a well-established shear failure criterion that is widely recognized and commonly used in engineering practice. It offers a reliable and easily obtainable set of parameters. Hence, we have chosen to employ the Mohr–Coulomb model in our simulations. The boundary conditions around the model are fixed, except for the surface of the Diaozui rock mass. That is, as shown in Fig. 6a, the left and right sides constrained the displacement in the X direction, the back side constrained in the Y direction, and the bottom constrained in the Z direction. According to the requirements of our study, a total of 54 sets of moderately weathered rock samples were carefully collected from the rock mass. These samples were then subjected to a series of comprehensive

physical and mechanical experiments. Through rigorous statistical analysis, we have successfully determined the essential parameters of the rock, which are summarized in Table 3. Additionally, the fracture parameters of L1, L2, L3, L4, and L5 were determined based on a combination of experimental measurements and relevant literature (Wang et al. 2020a, b). These fracture parameters have also been included in Table 3.

## Results and discussion

### Verification of the numerical analysis model

Through numerical calculations, we obtained data on the stress distribution of the Diaozui rock mass. The three-dimensional numerical analysis model of the Diaozui rock

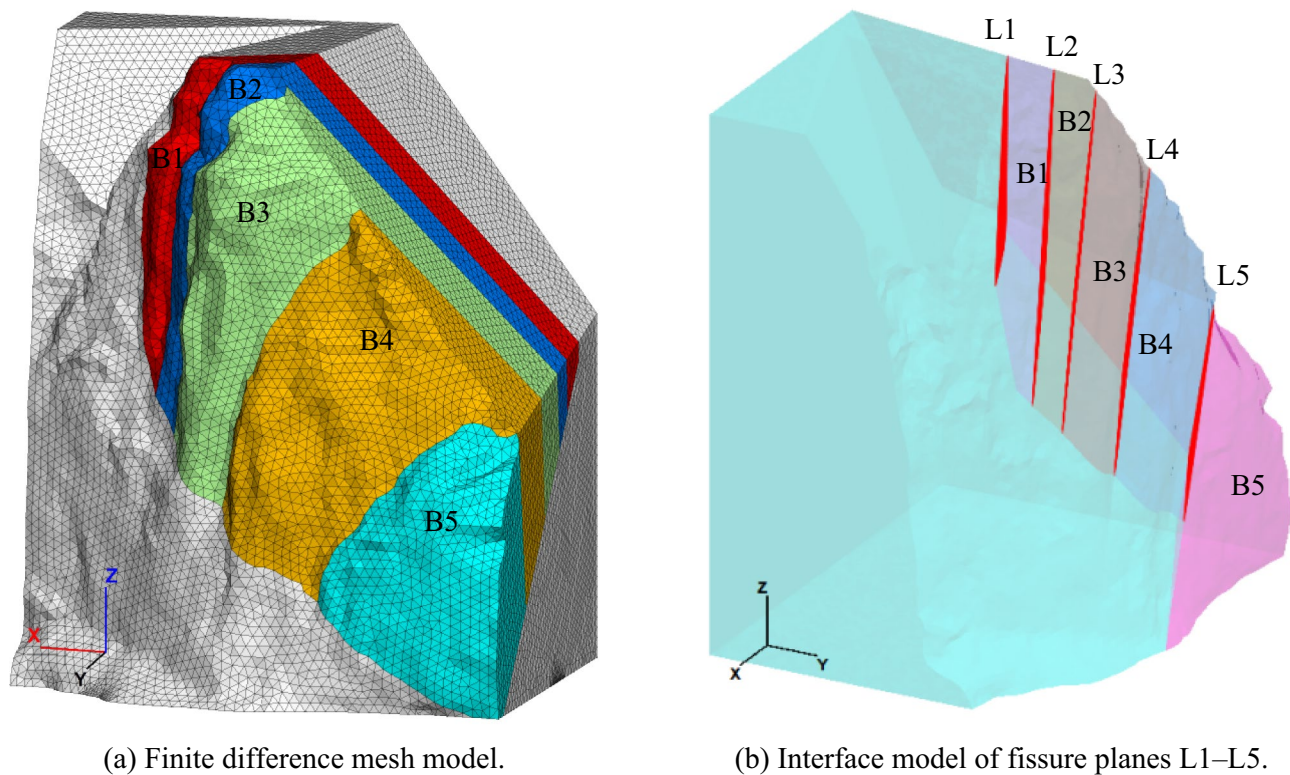
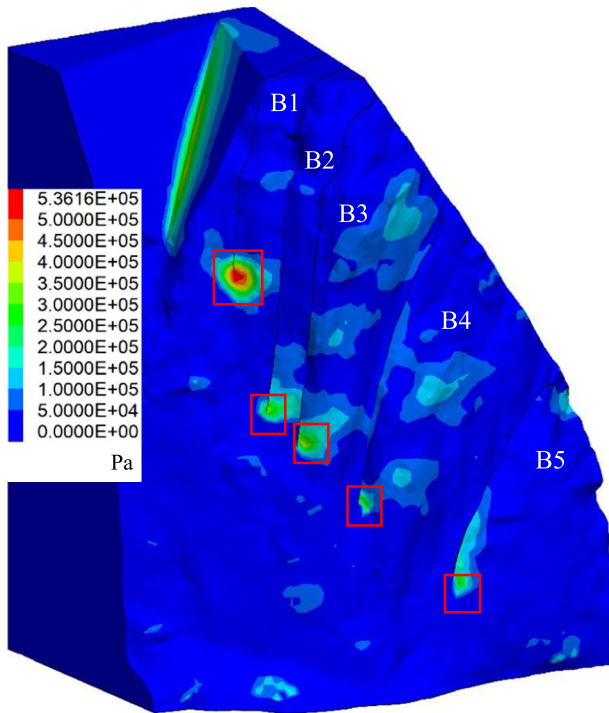


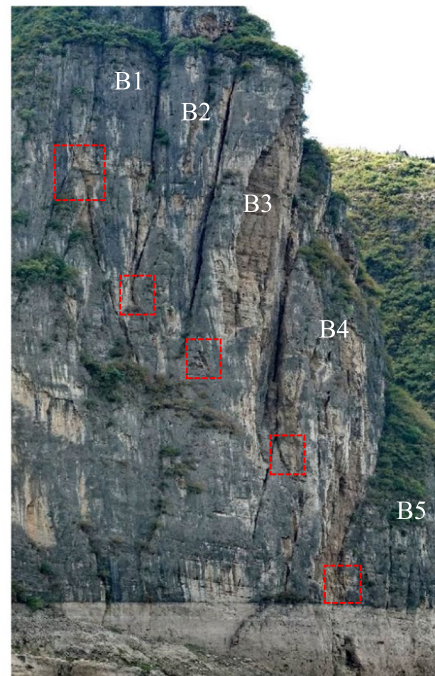
Fig. 6 3D numerical analysis model of the Diaozui rock mass

Table 3 Parameters of the rock mass and the fractures

Type	Density (kg/m <sup>3</sup> )	Elastic modulus (GPa)	Poisson's ratio	Normal stiffness (GPa)	Tangential stiffness (GPa)	Cohesion (MPa)	Friction angle (°)	Tensile strength (MPa)
Rock mass	2600	6.8	0.22	/	/	2.94	30.4	0.436
Fractures (interface)	/	/	/	19	19	0.050	18	0



(a) Tensile stress zone obtained by numerical calculation.



(b) Distribution of tensile cracks of Diaozi rock mass



(c) Crack at the bottom of rock B1.



(d) Crack at the bottom of rock B2.



(e) Crack at the bottom of rock B3.

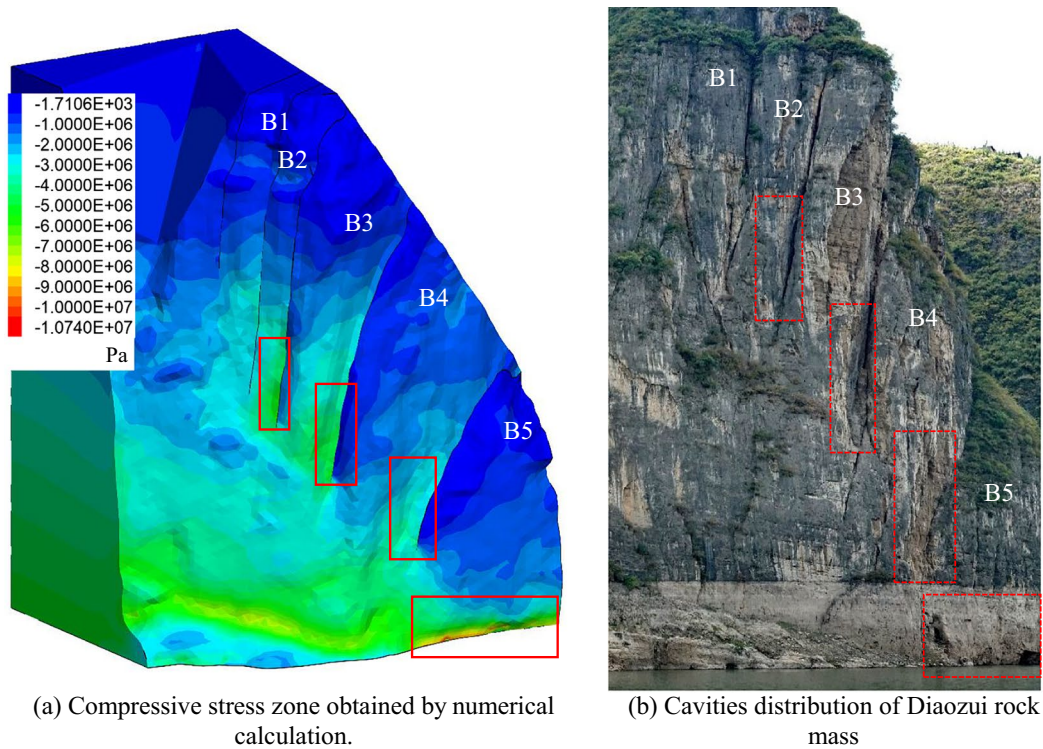


(f) Crack at the bottom of rock B4.



(g) Cracks at the bottom of rock B5.

**Fig. 7** Maximum principal stress (tensile stress) of the Diaozi rock mass simulation versus that of field investigation



(c) Rock block B2 is compressed and falling to form a cavity.



(d) Rock block B3 is compressed and falling to form a cavity.



(e) Rock block B4 is compressed and falling to form a cavity.



(f) Rock block B5 is compressed and falling to form a cavity.

**Fig. 8** Minimum principal stress (compressive stress) of Diaozui rock mass simulation versus that of field investigation

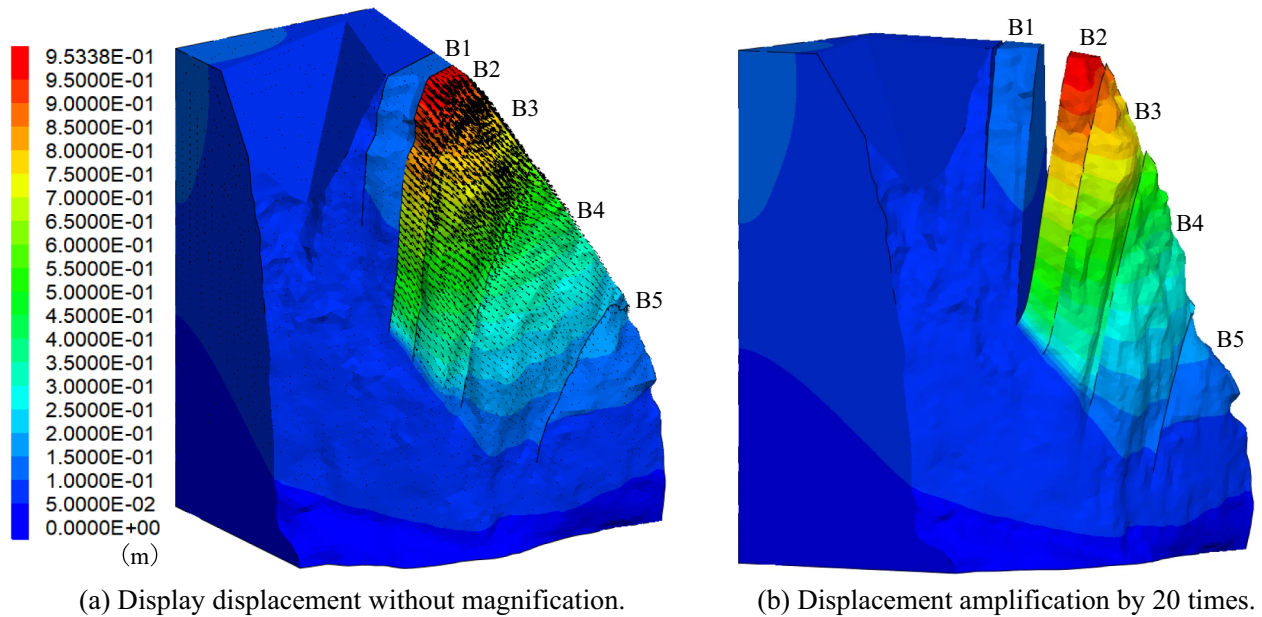


**Fig. 9** Value and vector of displacement in the limit state of Diaozui rock mass

mass was verified by comparing their deformation characteristics with the numerical analysis results.

Figure 7a shows the tensile stress distribution of Diaozui rock mass determined through numerical calculations, which was primarily distributed in the inner side of B1, B2, B3, B4, and B5 bases, ranged from 300 to 536 kPa, and marked in red boxes in Fig. 7a. Through on-site investigation, we found that obvious oblique tensile cracks (as shown in Fig. 7b, marked in red boxes) appeared at the base of the rock blocks B1, B2, B3, B4, and B5. The photos and characteristics of these cracks are shown in Figs. 7c, d, e, f, and g, respectively. The crack directions at these five locations are consistent, with a dip angle of approximately 70–80°. The location area of these cracks corresponds exactly to the high tensile stress zone of the numerical calculation results shown in Fig. 7a, and the direction of these cracks also corresponds to the calculated tensile direction.

The numerical calculation results show that the maximum principal stress (compressive stress) of the Diaozui rock mass was mainly distributed on the outer part of B2, B3, B4, and B5 bases, as well as at the bottom of the rock mass, as shown in Fig. 8a, with a value range of about 5 to 10 MPa, marked in red boxes. According to the on-site investigation results, signs of crushing and falling blocks were found in the area corresponding to the high-pressure stress zone of the numerical calculation results (Fig. 8a), as shown in Fig. 8b, marked in red boxes. Cracks formed by crushing and falling blocks appear on the outside of the B2 base, as shown in Fig. 8c. A long strip shaped cavity was formed by crushing the falling blocks on the outside

of the B3 base, as shown in Fig. 8d. In the high-compressive stress area on the outside of the B4 base, signs of crushing and falling blocks were found, and a large cavity was formed there (Fig. 8e). The pressure was supposed to be concentrated at the B5 base, resulting from the rock collapse due to pressure concentration (Fig. 8f).

The numerical simulation stress calculations of Diaozui rock mass explain the observed deformation and failure phenomena, which verified the three-dimensional numerical analysis model of the Diaozui rock mass.

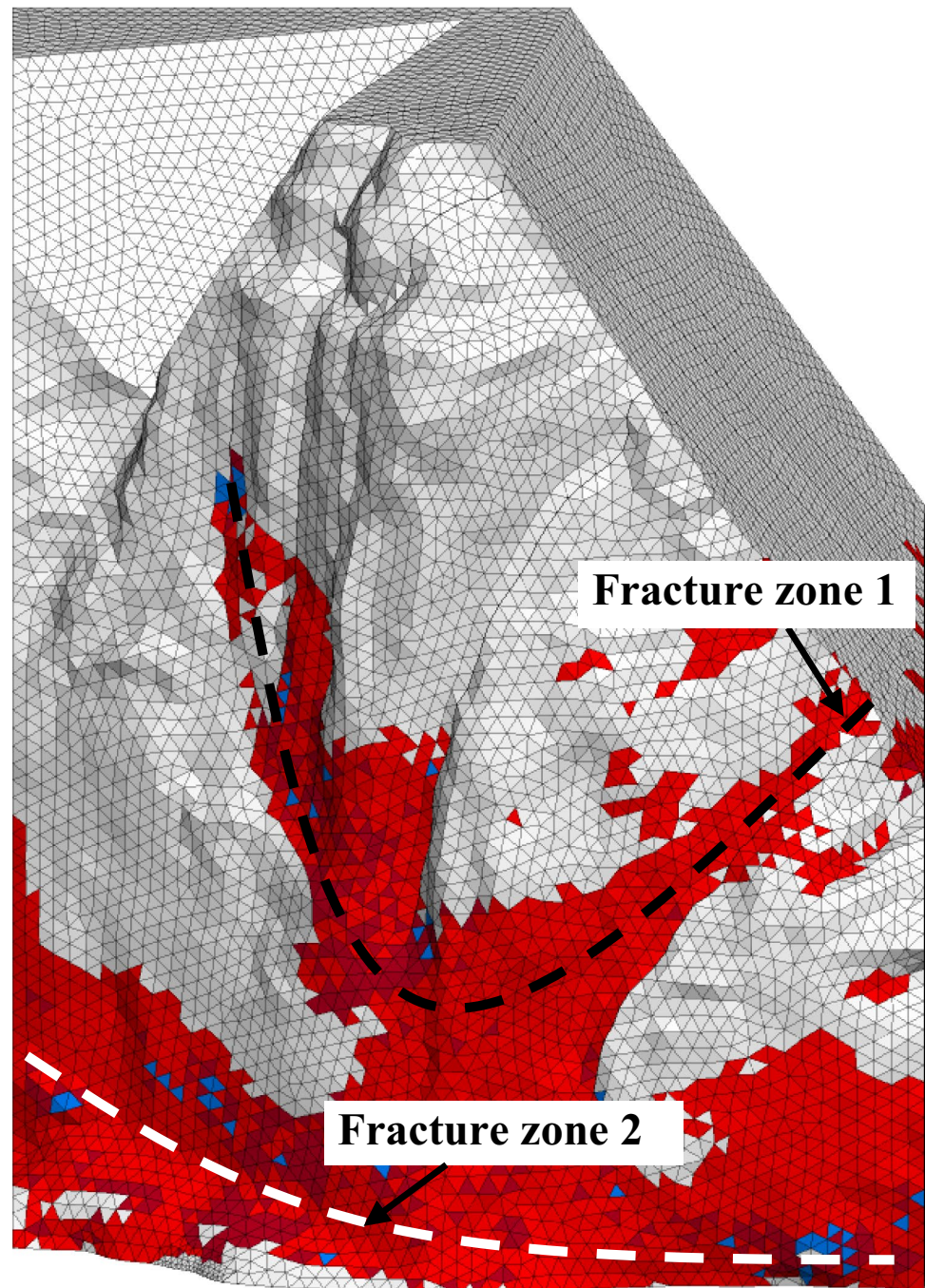
### Deformation evolution law under the limit state

This study was based on the Strength reduction method (SRM) to study the deformation and failure laws of the hazardous Diaozui rock mass. In this numerical analysis, the internal friction angle and cohesion of the rock mass were simultaneously reduced until the rock mass was in a critical unstable state. Then, by analyzing the stress and deformation characteristics of the critical failure of the rock mass, the failure mode and deformation evolution law were studied. When the reduction coefficient was reduced to 1.89, the hazardous Diaozui rock mass was in a critical unstable state.

### Displacement analysis

Figure 9 shows that rock mass displacement occurred in B2, B3, and B4. The displacement vector primarily

**Fig. 10** Distribution of the plastic zone



changed along the change in the direction of fissures L2, L3, and L4 in B2, B3, and B4, respectively, to the north. The displacement of B1 and B5 was slight, showing that B1 and B5 have good self-stability.

#### Failure analysis

Figure 10 shows the plastic zone distribution of the rock mass obtained through numerical calculations when the

strength was reduced to the limit state. The plastic zone in Fig. 10 mainly consists of two regions, namely plastic zone 1 and plastic zone 2. The distribution of plastic zone 1 is primarily distributed at the base of B1, B2, B3, B4, and B5, which is consistent with the shear strain distribution in Fig. 11. The plastic zone 1 developed from the base of B1 to that of B2, B3, and B4 and penetrated the middle of B4. Therefore, there is a possibility to form a failure surface along the base of B2, B3, and the middle and lower parts of B4 under the limit state.

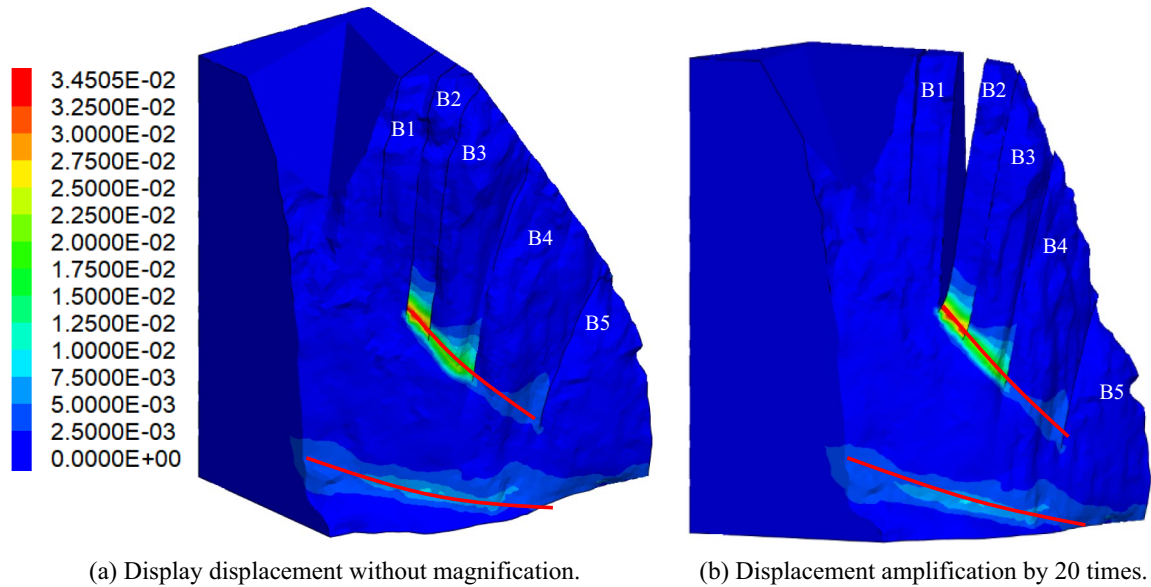


**Fig. 11** Shear strain in the limit state of Diaozui rock mass

**Table 4** Simulation of the peeling process of rockfall No. B4

Calculation condition	Volume of rockfall mass (m <sup>3</sup> )	Accumulated volume of rockfall mass (m <sup>3</sup> )
First peeling	2100	2100
Second peeling	2700	4800
Third peeling	4590	9390
Fourth peeling	2400	11,790
Fifth peeling	3200	14,990
Sixth peeling	2800	17,790
Seventh peeling	5100	22,890

Figure 11 illustrates the shear strain of the rock mass obtained through the numerical calculation when the strength was reduced to the limit state. The shear strain was mainly concentrated at the base of B2, B3, and B4 and at the bottom of the whole rock mass. The shear strain developed and penetrated through the bases of B2, B3, and B4. The strain was the greatest at the B2 base, followed by the B3 base, and the lowest at the B4 base; therefore, B1 can achieve self-stability through strength reduction while B2 acts on B3, B3 acts on B4, and B4 acts on B5 under the limit state. B2, B3, B4, and B5 are not completely penetrated under the limit state but sheared out from B4, which is consistent with the results of plastic zone distribution. During strength reduction, B4 acted as a key plate in supporting B2 and B3 with low self-stability.

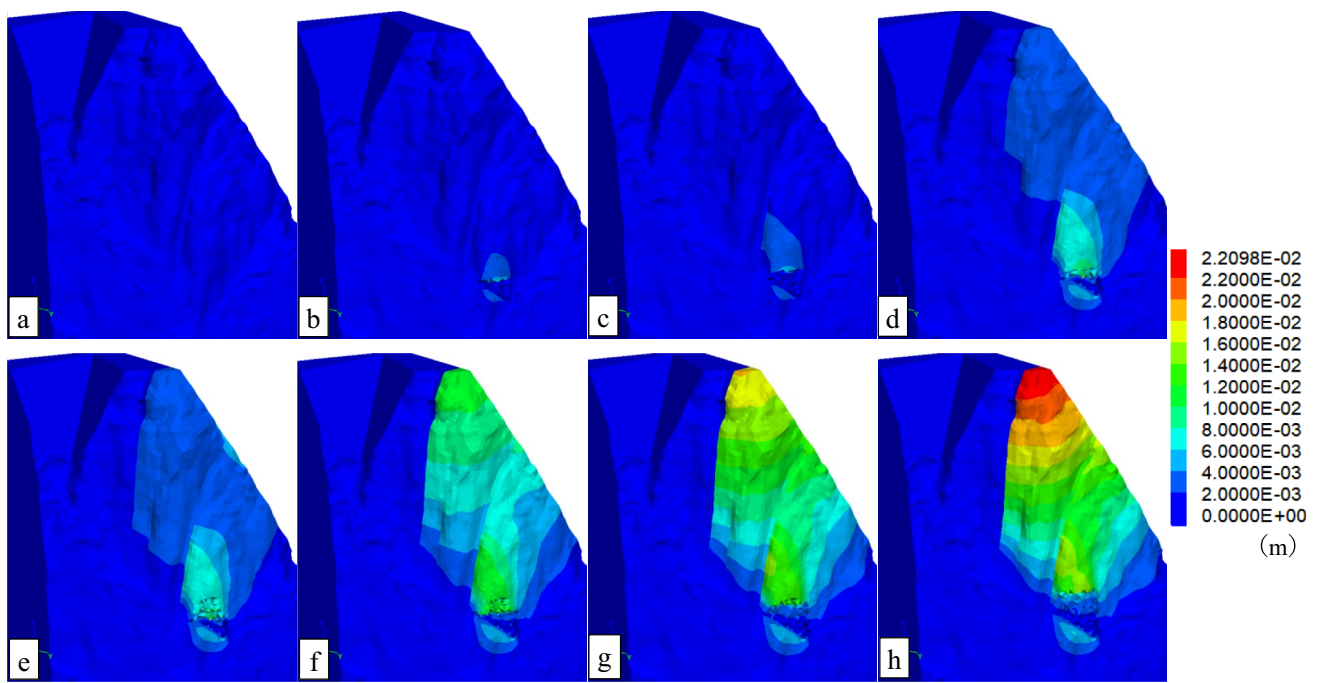
The distribution of plastic zone 2 is at the bottom of the entire Diaozui rock mass, which is consistent with the shear strain distribution in Fig. 11. The penetrating area of the plastic zone was relatively large at the bottom of the entire

rock mass, indicating that it is likely to establish a failure model for the bottom of the whole Diaozui rock mass under the limit state. The shear strain at plastic zone 2 is generally smaller than that at plastic zone 1. This indicates that the overall stability of the Diaozui rock mass is controlled by the strength of the B2, B3, B4, and B5 bases. Plastic zone 1 plays a major controlling role in the hazardous Diaozui rock mass.

### Rockfall collapse analysis

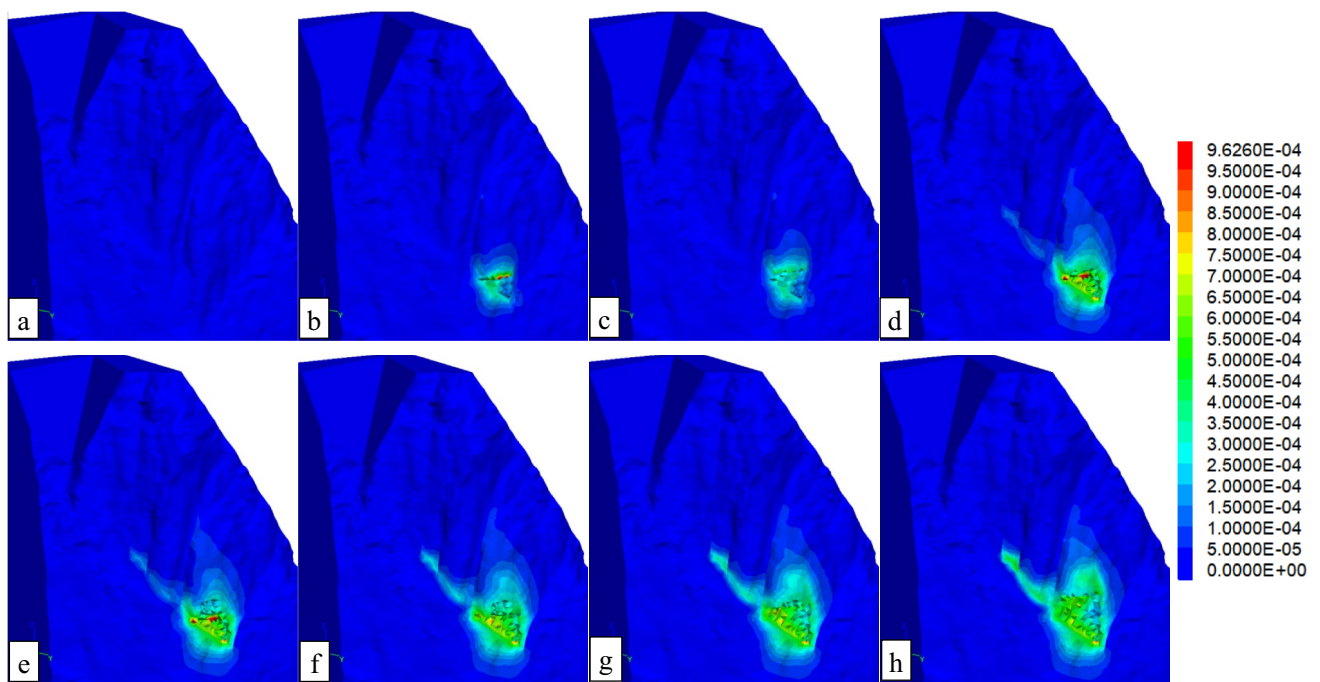
According to the investigation, a large cavity was formed on the outside of the B4 base after rock blocks peeled off, and, recently, the rock collapse occurred in the cavity. As the surface rock mass of B4 gradually collapses, the stability of the Diaozui rock mass will inevitably be affected; therefore, we simulated the stress and deformation response of the Diaozui rock mass during their gradual peeling off the B4 base to predict their influence on the development of instability in the Diaozui rock mass. According to the distribution and combination of rock fractures, the hypothetical volume of rockfall that may occur in the future can be estimated (Mavrouli and Corominas 2017). Based on the fractures in the cavity of the B4 base, the possible process and volume of rock peeling in the future are estimated. As shown in Table 4, the gradual peeling process of the B4 base was divided into seven calculation conditions.

Figure 12 shows the calculated displacement of the rock mass during the peeling process of the B4 base. With an increase in the number of rocks peeling off the B4 base, the displacement range and value of the rock mass model gradually increased. When the fifth peeling was calculated, the



**Fig. 12** Displacement of the Diaozui rock mass during the simulation of the peeling process of rock B4. **a** Initial displacement field. **b** Displacement field of the first peeling. **c** Displacement field of the second peeling. **d** Displacement field of the third peeling. **e** Displacement

field of the fourth peeling. **f** Displacement field of the fifth peeling. **g** Displacement field of the sixth peeling. **h** Displacement field of the seventh peeling



**Fig. 13** Shear strain development in Diaozui rock mass during the simulation of the peeling process of rock B4. **a** Initial model. **b** Shear strain of the first peeling. **c** Shear strain of the second peeling.

**d** Shear strain of the third peeling. **e** Shear strain of the fourth peeling. **f** Shear strain of the fifth peeling. **g** Shear strain of the sixth peeling. **h** Shear strain of the seventh peeling

maximum displacement of the model was transferred from the B4's peeling area to the B2's top. This indicates a radical change in the displacement field of rock mass after the fifth peeling. The local displacement field generated by peeling was transformed into a potential field that influences the entire rock mass. When the seventh peeling was calculated, the maximum displacement evidently changed to the B2's top.

Figure 13 shows the shear strain of the rock mass during the peeling process of the B4 base. With an increase in the number of rocks peeling off the B4 base, the shear strain of the model gradually increased along the peeling position. During the peeling process of the B4 base, the shear strain of the model evidently increased along the base of plate-like rock blocks B2 and B3 and finally formed a penetration zone.

Therefore, overall, instability was observed in Diaozui rock mass when the rocks peeled off the B4 base for the fifth time (with a cumulative peeling volume of 14,990 m<sup>3</sup>).

## Conclusion

In this study, we aimed to evaluate the hazardous Diaozui rock mass in the Qutang Gorge in the Three Gorges Reservoir area of the Yangtze River to prevent rockfall, and we proposed a methodological approach for the analysis of the stability conditions of a hazardous rock mass. We established a three-dimensional geological model and a three-dimensional numerical analysis model of the hazardous rock mass based on the data obtained using a field survey and tilt photography. The SRM was used to analyse the hazardous rock mass under the limit state, and the peeling processes of the rock mass were simulated. The numerical analysis of the failure evolution process of the hazardous Diaozui rock mass was performed. The following conclusions were drawn:

- 1) The stability of B1 and B5 was better, followed by that of B2, B3, and B4. Under the limit state, the hazardous Diaozui rock mass primarily failed along the bases of B2, B3, and B4 and penetrated the middle and lower parts along B4. The force of B2 acted on B3 and was subsequently transmitted to B3 and B4.
- 2) Under the limit state, B4 of the hazardous Diaozui rock mass acted as the key plate in supporting B2 and B3 with low self-stability.
- 3) With a greater number of rocks peeling off the B4 base, the displacement range and value of the rocks gradually increased. Furthermore, the shear strain gradually increased along the B2 and B3 bases and finally formed a penetration zone. When the cumulative peeling volume of B4 reached 14,990 m<sup>3</sup>, the local displacement field generated by the peeling area transformed into a scale field that influenced the entire rock mass, resulting in the overall instability of the Diaozui rock mass.

**Acknowledgements** The authors acknowledge financial support of the project (CSTB2022NSCQ-MSX1466, cstc2021jcyj-msxmX1039) supported by the Natural Science Foundation of Chongqing and the project (KJ2021050) supported by the Chongqing Geological Disaster Prevention Center.

**Data availability** Data supporting the results of this study are available from the corresponding author, Qiang Xie.

## Declarations

**Conflict of interest** The authors declare no competing interests.

## References

- Abu Seif E-SS, Bahabri AA (2019) Rockfall hazards assessment along the Aswan–Cairo highway, Sohag Governorate, Upper Egypt. *Nat Hazards* 99:991–1005. <https://doi.org/10.1007/s11069-019-03788-w>
- Antoniou AA, Lekkas E (2010) Rockfall susceptibility map for Athinios port, Santorini Island. *Greece Geomorphology* 118:152–166. <https://doi.org/10.1016/j.geomorph.2009.12.015>
- Azzoni A, de Freitas MH (1995) Experimentally gained parameters, decisive for rock fall analysis. *Rock Mech Rock Eng* 28:111–124. <https://doi.org/10.1007/BF01020064>
- Bolin H, Lide C, Xuanming P, Guanning L, Xiaoting C, Haogang D, Tianci L (2010) Assessment of the risk of rockfalls in Wu Gorge, Three gorges. *China Landslides* 7:1–11. <https://doi.org/10.1007/s10346-009-0170-7>
- Congress SSC, Puppala AJ (2021) Geotechnical slope stability and rockfall debris related safety assessments of rock cuts adjacent to a rail track using aerial photogrammetry data analysis. *Transp Geotech* 30:100595. <https://doi.org/10.1016/j.trgeo.2021.100595>
- Daghigh H, Tannant DD, Daghigh V, Lichti DD, Lindenbergh R (2022) A critical review of discontinuity plane extraction from 3D point cloud data of rock mass surfaces *Comput Geosci* 169:105241. <https://doi.org/10.1016/j.cageo.2022.105241>
- Farmakis I, DiFrancesco P-M, Hutchinson DJ, Vlachopoulos N (2022) Rockfall detection using LiDAR and deep learning. *Eng Geol* 309:106836. <https://doi.org/10.1016/j.enggeo.2022.106836>
- Feng Z, Li B, Yin YP, He K (2014) Rockslides on limestone cliffs with subhorizontal bedding in the southwestern calcareous area of China. *Nat Hazards Earth Syst Sci* 14:2627–2635. <https://doi.org/10.5194/nhess-14-2627-2014>
- Huang B, Yin Y, Liu G, Wang S, Chen X, Huo Z (2012) Analysis of waves generated by Gongjiafang landslide in Wu Gorge, three Gorges reservoir, on November 23, 2008. *Landslides* 9:395–405. <https://doi.org/10.1007/s10346-012-0331-y>
- Huang B, Yin Y, Tan J (2019) Risk assessment for landslide-induced impulse waves in the Three Gorges Reservoir, China. *Landslides* 16:585–596. <https://doi.org/10.1007/s10346-018-1115-9>
- Lambert S, Bourrier F (2013) Design of rockfall protection embankments: a review. *Eng Geol* 154:77–88. <https://doi.org/10.1016/j.enggeo.2012.12.012>
- Li X, Chen J, Zhu H (2016) A new method for automated discontinuity trace mapping on rock mass 3D surface model. *Comput Geosci* 89:118–131. <https://doi.org/10.1016/j.cageo.2015.12.010>
- Mavrouli O, Corominas J (2017) Comparing rockfall scar volumes and kinematically detachable rock masses. *Eng Geol* 219:64–73. <https://doi.org/10.1016/j.enggeo.2016.08.013>
- Menegoni N, Giordan D, Perotti C, Tannant DD (2019) Detection and geometric characterization of rock mass discontinuities using a

- 3D high-resolution digital outcrop model generated from RPAS imagery – ormea rock slope, Italy. *Eng Geol* 252:145–163. <https://doi.org/10.1016/j.enggeo.2019.02.028>
- Menk J, Berger F, Moos C, Dorren L (2023) Towards an improved rapid assessment tool for rockfall protection forests using field-mapped deposited rocks. *Geomorphology* 422:108520. <https://doi.org/10.1016/j.geomorph.2022.108520>
- Perera JS, Lam N (2023) Rockfall protection wall that can withstand multiple strikes without needing to be repaired. *Int J Impact Eng* 173:104476. <https://doi.org/10.1016/j.ijimpeng.2022.104476>
- Pignatola A, Forte G, Budetta P, Santo A (2022) Topographic amplification and debris remobilization as a cause for increasing rockfall hazard in seismic areas: a case study in Central Italy. *Geomorphology* 403:108160. <https://doi.org/10.1016/j.geomorph.2022.108160>
- Schilirò L, Robiati C, Smeraglia L, Vinci F, Iannace A, Parente M, Tavani S (2022) An integrated approach for the reconstruction of rockfall scenarios from UAV and satellite-based data in the Sorrento Peninsula (southern Italy). *Eng Geol* 308:106795. <https://doi.org/10.1016/j.enggeo.2022.106795>
- Singh PK, Wasnik AB, Kainthola A, Sazid M, Singh TN (2013) The stability of road cut cliff face along SH-121: a case study. *Nat Hazards* 68:497–507. <https://doi.org/10.1007/s11069-013-0627-9>
- Sun C, Chai J, Xu Z, Qin Y, Chen X (2016) Stability charts for rock mass slopes based on the Hoek-Brown strength reduction technique. *Eng Geol* 214:94–106. <https://doi.org/10.1016/j.enggeo.2016.09.017>
- Umili G, Ferrero A, Einstein HH (2013) A new method for automatic discontinuity traces sampling on rock mass 3D model. *Comput Geosci* 51:182–192. <https://doi.org/10.1016/j.cageo.2012.07.026>
- Verma AK, Sardana S, Sharma P, Dinpuia L, Singh TN (2019) Investigation of rockfall-prone road cut slope near Lengpui Airport, Mizoram, India. *J Rock Mech Geotech Eng* 11:146–158. <https://doi.org/10.1016/j.jrmge.2018.07.007>
- Wang Y, Liu J, Li D, Yan S (2017) Optimization model for maximum tsunami amplitude generated by riverfront landslides based on laboratory investigations. *Ocean Eng* 142:433–440. <https://doi.org/10.1016/j.oceaneng.2017.07.030>
- Wang L, Huang B, Zhang Z, Dai Z, Zhao P, Hu M (2020a) The analysis of slippage failure of the HuangNanBei slope under dry-wet cycles in the three gorges reservoir region, China. *Geomatics Nat Hazards Risk* 11:1233–1249. <https://doi.org/10.1080/19475705.2020.1785554>
- Wang L, Yin Y, Huang B, Zhang Z, Zhao P, Wei Y (2020b) A study of the treatment of a dangerous thick submerged rock mass in the three gorges reservoir area. *Bull Eng Geol Environ* 79:2579–2590. <https://doi.org/10.1007/s10064-020-01724-y>
- Wang W, Zhao W, Chai B, Du J, Tang L, Yi X (2022) Discontinuity interpretation and identification of potential rockfalls for high-steep slopes based on UAV nap-of-the-object photogrammetry. *Comput Geosci* 166:105191. <https://doi.org/10.1016/j.cageo.2022.105191>
- Yan J, Chen J, Tan C, Zhang Y, Liu Y, Zhao X, Wang Q (2023) Rockfall source areas identification at local scale by integrating discontinuity-based threshold slope angle and rockfall trajectory analyses. *Eng Geol* 313:106993. <https://doi.org/10.1016/j.enggeo.2023.106993>
- Yang Y, Chen T, Wu W, Zheng H (2021a) Modelling the stability of a soil-rock-mixture slope based on the digital image technology and strength reduction numerical manifold method. *Eng Anal Boundary Elem* 126:45–54. <https://doi.org/10.1016/jenganabound.2021.02.008>
- Yang Y, Xia Y, Zheng H, Liu Z (2021b) Investigation of rock slope stability using a 3D nonlinear strength-reduction numerical manifold method. *Eng Geol* 292:106285. <https://doi.org/10.1016/j.enggeo.2021.106285>
- Yin Y, Huang B, Wang W, Wei Y, Ma X, Ma F, Zhao C (2016) Reservoir-induced landslides and risk control in three gorges Project on Yangtze River, China. *J Rock Mech Geotech Eng* 8:577–595. <https://doi.org/10.1016/j.jrmge.2016.08.001>
- Zhang Y, Li D, Chen L, Yin K, Xiao L, Fu X, Glade T, Leo C (2020) Numerical analysis of landslide-generated impulse waves affected by the reservoir geometry. *Eng Geol* 266:105390. <https://doi.org/10.1016/j.enggeo.2019.105390>
- Zhang W, Zhao X, Pan X, Wei M, Yan J, Chen J (2022) Characterization of high and steep slopes and 3D rockfall statistical kinematic analysis for Kangyuyu area, China. *Eng Geol* 308:106807. <https://doi.org/10.1016/j.enggeo.2022.106807>
- Zheng Y, Tang X, Zhao S, Deng C, Lei W (2009) Strength reduction and step-loading finite element approaches in geotechnical engineering. *J Rock Mech Geotech Eng* 1:21–30. <https://doi.org/10.3724/SPJ.1235.2009.00021>
- Zheng D, Frost JD, Huang RQ, Liu FZ (2015) Failure process and modes of rockfall induced by underground mining: a case study of Kaiyang Phosphorite Mine rockfalls. *Eng Geol* 197:145–157. <https://doi.org/10.1016/j.enggeo.2015.08.011>
- Zienkiewicz OC, Humpheson C, Lewis RW (1975) Associated and non-associated visco-plasticity and plasticity in soil mechanics. *Géotechnique* 25:671–689. <https://doi.org/10.1680/geot.1975.25.4.671>

**Publisher's Note** Springer Nature remains neutral with regard to jurisdictional claims in published maps and institutional affiliations.